

Blind Compressive Sensing Dynamic MRI

Sajan Goud Lingala*, *Student Member, IEEE*, and Mathews Jacob, *Senior Member, IEEE*

Abstract—We propose a novel blind compressive sensing (BCS) frame work to recover dynamic magnetic resonance images from undersampled measurements. This scheme models the dynamic signal as a sparse linear combination of temporal basis functions, chosen from a large dictionary. In contrast to classical compressed sensing, the BCS scheme simultaneously estimates the dictionary and the sparse coefficients from the undersampled measurements. Apart from the sparsity of the coefficients, the key difference of the BCS scheme with current low rank methods is the nonorthogonal nature of the dictionary basis functions. Since the number of degrees-of-freedom of the BCS model is smaller than that of the low-rank methods, it provides improved reconstructions at high acceleration rates. We formulate the reconstruction as a constrained optimization problem; the objective function is the linear combination of a data consistency term and sparsity promoting ℓ_1 prior of the coefficients. The Frobenius norm dictionary constraint is used to avoid scale ambiguity. We introduce a simple and efficient majorize–minimize algorithm, which decouples the original criterion into three simpler subproblems. An alternating minimization strategy is used, where we cycle through the minimization of three simpler problems. This algorithm is seen to be considerably faster than approaches that alternates between sparse coding and dictionary estimation, as well as the extension of K-SVD dictionary learning scheme. The use of the ℓ_1 penalty and Frobenius norm dictionary constraint enables the attenuation of insignificant basis functions compared to the ℓ_0 norm and column norm constraint assumed in most dictionary learning algorithms; this is especially important since the number of basis functions that can be reliably estimated is restricted by the available measurements. We also observe that the proposed scheme is more robust to local minima compared to K-SVD method, which relies on greedy sparse coding. Our phase transition experiments demonstrate that the BCS scheme provides much better recovery rates than classical Fourier-based CS schemes, while being only marginally worse than the dictionary aware setting. Since the overhead in additionally estimating the dictionary is low, this method can be very useful in dynamic magnetic resonance imaging applications, where the signal is not sparse in known dictionaries. We demonstrate the utility of the BCS scheme in accelerating contrast enhanced dynamic data. We observe superior reconstruction performance with the BCS scheme in comparison to existing low rank and compressed sensing schemes.

Index Terms—Blind compressed sensing (BCS), dynamic magnetic resonance imaging (DMRI), undersampled reconstruction.

Manuscript received January 10, 2013; revised March 20, 2013; accepted March 22, 2013. Date of publication March 27, 2013; date of current version May 29, 2013. This work is supported in part by the National Science Foundation (NSF) under Grant CCF-0844812 and Grant CCF 1116067, in part by National Institute of Health (NIH) under Grant 1R21HL109710-1A1, and in part by the American Heart Association (AHA) under Grant 12 PRE11920052. Asterisk indicates corresponding author.

*S. G. Lingala is with the Department of Biomedical Engineering, The University of Iowa, IA 52242 USA (e-mail: sajangoud-lingala@uiowa.edu).

M. Jacob is with the Department of Electrical and Computer Engineering, The University of Iowa, IA 52242 USA.

Color versions of one or more of the figures in this paper are available online at <http://ieeexplore.ieee.org>.

Digital Object Identifier 10.1109/TMI.2013.2255133

I. INTRODUCTION

DYNAMIC magnetic resonance imaging MRI (DMRI) is a key component of many clinical exams such as cardiac, perfusion, and functional imaging. The slow nature of the MR image acquisition scheme and the risk of peripheral nerve stimulation often restricts the achievable spatio-temporal resolution and volume coverage in DMRI. To overcome these problems, several image acceleration schemes that recover dynamic images from undersampled $k-t$ measurements have been proposed. Since the recovery from undersampled data is ill-posed, these methods exploit the compact representation of the spatio-temporal signal in a specified basis/dictionary to constrain the reconstructions. For example, breath-held cardiac cine acceleration schemes model the temporal intensity profiles of each voxel as a linear combination of a few Fourier exponentials to exploit the periodicity of the spatio-temporal data. While early models preselect the specific Fourier basis functions using training data (e.g., [1]–[4]), more recent algorithms rely on compressive sensing (CS) (e.g., [5]–[7]). These schemes demonstrated high acceleration factors in applications involving periodic/quasi periodic temporal patterns. However, the straightforward extension of these algorithms to applications such as free breathing myocardial perfusion MRI and free breathing cine often results in poor performance since the spatio-temporal signal is not periodic; many Fourier basis functions are often required to represent the voxel intensity profiles [8], [9]. To overcome this problem, several researchers have recently proposed to simultaneously estimate an orthogonal dictionary of temporal basis functions (possibly non-Fourier) and their coefficients directly from the undersampled data [10]–[13]; these methods rely on the low-rank structure of the spatio-temporal data to make the above estimation well posed. Since the basis functions are estimated from the data itself and no sparsity assumption is made on the coefficients, these schemes can be thought of blind linear models (BLMs). These methods have been demonstrated to provide considerably improved results in perfusion [13]–[15] and other real time applications [16]. One challenge associated with this scheme is the degradation in performance in the presence of large inter-frame motion. Specifically, large numbers of temporal basis functions are needed to accurately represent the temporal dynamics, thus restricting the possible acceleration. In such scenarios, these methods result in considerable spatio-temporal blurring at high accelerations [13], [17], [18]. The number of degrees-of-freedom in the low-rank representation is approximately¹ Mr , where M is the number of pixels and r is number of temporal basis functions or the rank. The dependence of the degrees-of-freedom on the number of temporal basis function is

¹ Assuming that the number of pixels is far greater than the number of frames, which is generally true in dynamic imaging applications.

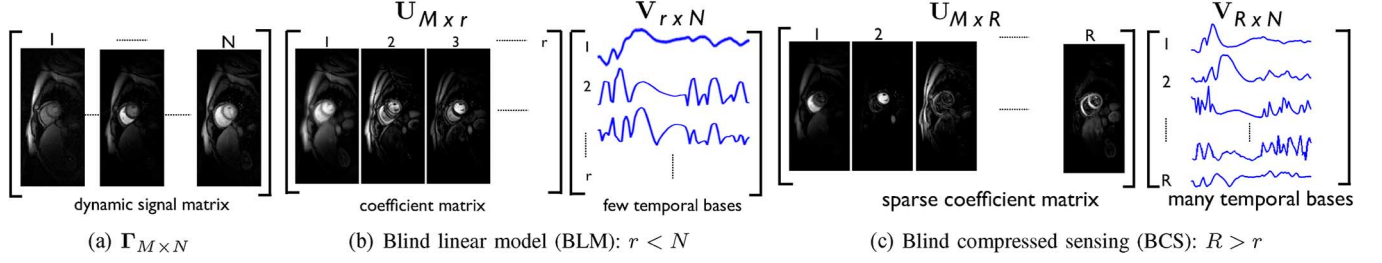


Fig. 1. Comparison of BCS and BLM representations of dynamic imaging data: The Casorati form of the dynamic signal Γ is shown in (a). The BLM and BCS decompositions of Γ are respectively shown in (b) and (c). BCS uses a large over-complete dictionary, unlike the orthogonal dictionary with few basis functions in BLM; ($R > r$). Note that the coefficients/spatial weights in BCS are sparser than that of BLM. The temporal basis functions in the BCS dictionary are representative of specific regions, since they are not constrained to be orthogonal. For example, the first, second columns of $U_{M \times R}$ in BCS correspond respectively to the temporal dynamics of the right and left ventricles in this myocardial perfusion data with motion. We observe that only 4–5 coefficients per pixel are sufficient to represent the dataset.

the main reason for the tradeoff between accuracy and achievable acceleration in applications with large motion.

We introduce a novel dynamic imaging scheme, termed as blind compressed sensing (BCS), to improve the recovery of dynamic imaging datasets with large inter-frame motion. Similar to classical CS schemes [5]–[7], the voxel intensity profiles are modeled as a sparse linear combination of basis functions in a dictionary. However, instead of assuming a fixed dictionary, the BCS scheme estimates the dictionary from the undersampled measurements itself. While this approach of estimating the coefficients and dictionary from the data is similar to BLM methods, the main difference is the sparsity assumption on the coefficients. In addition, the dictionary in BCS is much larger and the temporal basis functions are not constrained to be orthogonal (see Fig. 1). The significantly larger number of basis functions in the BCS dictionary considerably improves the approximation of the dynamic signal, especially for datasets with significant inter-frame motion. The number of degrees-of-freedom of the BCS scheme is $Mk + RN - 1$, where k is the average sparsity of the representation, R is the number of temporal basis functions in the dictionary, and N is the total number of time frames. However, in dynamic MRI, since $M \gg N$ the degrees-of-freedom is dominated by the average sparsity k and not the dictionary size R , for reasonable dictionary sizes. In contrast to BLM, since the degrees-of-freedom in BCS is not heavily dependent on the number of basis functions, the representation is richer and hence provide an improved trade-off between accuracy and achievable acceleration.

An efficient computational algorithm to solve for the sparse coefficients and the dictionary is introduced in this paper. In the BCS representation, the signal matrix Γ is modeled as the product $\Gamma = UV$, where U is the sparse coefficient matrix V is the temporal dictionary. The recovery is formulated as a constrained optimization problem, where the criterion is a linear combination of the data consistency term and a sparsity promoting ℓ_1 prior on U , subject to a Frobenius norm (energy) constraint on V . We solve for U and V using a majorize–minimize framework. Specifically, we decompose the original optimization problem into three simpler problems. An alternating minimization strategy is used, where we cycle through the minimization of three simpler problems. The comparison of the proposed algorithm with a scheme that alternates between sparse coding and dictionary estimation demonstrates the computa-

tional efficiency of the proposed framework; both methods converge to the same minimum, while the proposed scheme is approximately ten times faster. We also observe that the proposed scheme is less sensitive to initial guesses, compared to the extension of the K-SVD scheme [19] to under-sampled dynamic MRI setting. It is seen that the ℓ_1 sparsity norm and Frobenius norm dictionary constraint enables the attenuation of insignificant dictionary basis functions, compared with the ℓ_0 sparsity norm and column norm dictionary constraint used by most dictionary learning schemes. This implicit model order selection property is important in the under sampled setting since the number of basis functions that can be reliably estimated is dependent on the available data and the signal to noise ratio.

The proposed work has some similarities to [20], where a patch dictionary is learned to exploit the correlations between image patches in a static image. The key difference is that the proposed scheme exploits the correlations between voxel time profiles in dynamic imaging rather than redundancies between image patches. The ℓ_0 norm sparsity constraints and unit column norm dictionary constraints are assumed in [20]. The adaptation of this formulation to our setting resulted in the learning of noisy basis functions at high acceleration factors. Similar to [21], the setting in [20] permits the reconstructed dataset to deviate from the sparse model. The denoising scheme is well-posed even in this relaxed setting since the authors assume overlapping patches; even if a patch does not have a sparse representation in the dictionary, the pixels in the patch are still constrained by the sparse representations of other patches containing them. Since there is no redundancy in our setting, the adaptation of the above scheme to our setting may also result in alias artifacts. Furthermore, the proposed numerical algorithm is very different from the optimization scheme in [20], where they alternate between a greedy K-SVD dictionary learning algorithm and a reconstruction update step admitting an efficient closed-form solution. We observe that the greedy approach is vulnerable to local minima in the dynamic imaging setting.

The proposed BCS setup has some key differences with the formulation in [22], where the recovery of several signals measured by the same sensing matrix is addressed; additional constraints on the dictionary were needed to ensure unique reconstruction in this setting. By contrast, we use different sensing matrices (sampling patterns) for different time frames, inspired by prior work in other dynamic MRI problems [5], [8], [13].

Our phase transition experiments show that we obtain good reconstructions without any additional constraints on the dictionary. Since the BCS scheme assumes that only very few basis functions are active at each voxel, this model can be thought of as a locally low-rank representation [17]. However, unlike [17], the BCS scheme does not estimate the basis functions for each neighborhood independently. Since it estimates \mathbf{V} from all voxels simultaneously, it is capable of exploiting the correlations between voxels that are well separated in space (nonlocal correlations).

II. DYNAMIC MRI RECONSTRUCTION USING THE BCS MODEL

A. Dynamic Image Acquisition

The main goal of the paper is to recover the dynamic dataset $\gamma(\mathbf{x}, t) : \mathbb{Z}^3 \rightarrow \mathbb{C}$ from its under-sampled Fourier measurements. We represent the dataset as the $M \times N$ Casorati matrix [10]

$$\mathbf{\Gamma}_{M \times N} = \begin{pmatrix} \gamma(\mathbf{x}_1, t_1) & \cdot & \cdot & \cdot & \gamma(\mathbf{x}_1, t_N) \\ \gamma(\mathbf{x}_2, t_1) & \cdot & \cdot & \cdot & \gamma(\mathbf{x}_2, t_N) \\ \cdot & \cdot & \cdot & \cdot & \cdot \\ \gamma(\mathbf{x}_M, t_1) & \cdot & \cdot & \cdot & \gamma(\mathbf{x}_M, t_N) \end{pmatrix}. \quad (1)$$

Here, M is the number of voxels in the image and N is the number of image frames in the dataset. The columns of $\mathbf{\Gamma}$ correspond to the voxels of each time frame. We model the measurement process as

$$\mathbf{b}_i = \underbrace{(\mathcal{S}_i \circ \mathcal{F} \circ \mathcal{T}_i)}_{\mathcal{A}_i}(\mathbf{\Gamma}) + \mathbf{n}_i; \quad i = 1, \dots, N \quad (2)$$

where \mathbf{b}_i and \mathbf{n}_i are, respectively, the measurement and noise vectors at the i th time instants. \mathcal{T}_i is an operator that extracts the i th column of $\mathbf{\Gamma}$, which corresponds to the image at t_i . \mathcal{F} is the 2-D Fourier transform and \mathcal{S}_i is the sampling operator that extracts the Fourier samples on the k-space trajectory corresponding to the i th time frame. We consider different sampling trajectories for different time frames to improve the diversity.

B. The BCS Representation

We model $\mathbf{\Gamma}$ as the product of a sparse coefficient matrix $\mathbf{U}_{M \times R}$ and a matrix $\mathbf{V}_{R \times N}$, which is a dictionary of temporal basis functions

$$\begin{aligned} & \underbrace{\begin{pmatrix} \gamma(\mathbf{x}_1, t_1) & \cdot & \cdot & \cdot & \gamma(\mathbf{x}_1, t_N) \\ \gamma(\mathbf{x}_2, t_1) & \cdot & \cdot & \cdot & \gamma(\mathbf{x}_2, t_N) \\ \cdot & \cdot & \cdot & \cdot & \cdot \\ \gamma(\mathbf{x}_M, t_1) & \cdot & \cdot & \cdot & \gamma(\mathbf{x}_M, t_N) \end{pmatrix}}_{\mathbf{\Gamma}_{M \times N}} \\ &= \underbrace{\begin{pmatrix} u_1(\mathbf{x}_1) & \cdot & \cdot & u_R(\mathbf{x}_1) \\ u_1(\mathbf{x}_2) & \cdot & \cdot & u_R(\mathbf{x}_2) \\ \cdot & \cdot & \cdot & \cdot \\ u_1(\mathbf{x}_M) & \cdot & \cdot & u_R(\mathbf{x}_M) \end{pmatrix}}_{\mathbf{U}_{M \times R}} \underbrace{\begin{pmatrix} v_1(t_1) & \cdot & \cdot & v_1(t_N) \\ v_2(t_1) & \cdot & \cdot & v_2(t_N) \\ \cdot & \cdot & \cdot & \cdot \\ v_R(t_1) & \cdot & \cdot & v_R(t_N) \end{pmatrix}}_{\mathbf{V}_{R \times N}}. \quad (3) \end{aligned}$$

Here, R is the total number of basis functions in the dictionary. The model in (3) can also be expressed as the partially separable function (PSF) model [10], [15]

$$\gamma(\mathbf{x}, t) = \sum_{i=1}^R u_i(\mathbf{x}) \mathbf{v}_i(t). \quad (4)$$

Here, $u_i(\mathbf{x})$ corresponds to the i th column of \mathbf{U} and is termed as the i th spatial weight. Similarly, $\mathbf{v}_i(t)$ corresponds to the i th row of \mathbf{V} and is the i th temporal basis function. The main difference with the traditional PSF setting is that the rows of \mathbf{U} are constrained to be sparse, which imply that there are very few nonzero entries; this also suggests that few of the temporal basis functions are sufficient to model the temporal profile at any specified voxel. The over-complete dictionary of basis functions are estimated from the data itself and are not necessarily orthogonal. In Fig. 1, we demonstrate the differences between BLM (low-rank) and BCS representations of a cardiac perfusion MRI data set with motion. Note that the sparsity constraint encourages the formation of voxel groups that share similar temporal profiles. Since many more basis functions are present in the dictionary, the representation is richer than the BLM model. The sparsity assumption ensures that the richness of the model is not translated to increased degrees-of-freedom. The sparsity assumption also enables the suppression of noise and blurring artifacts, thus resulting in sharper reconstructions.

The degrees-of-freedom associated with BCS is approximately $Mk + RN - 1$, where k is the average sparsity of the coefficients and R is the number of basis functions in the dictionary. Since $M \gg N$, the degrees-of-freedom in the BCS representation is dominated by the average sparsity (k) and not the size of the dictionary (R), for realistic dictionary sizes. Since the overhead in learning the dictionary is low, it is much better to learn the dictionary from the under-sampled data rather than using a suboptimal dictionary. Hence, we expect this scheme to provide superior results than classical compressive sensing schemes that use fixed dictionaries.

C. The Objective Function

We now address the recovery of the signal matrix $\mathbf{\Gamma}$, assuming the BCS model specified by (3). Similar to classical compressive sensing schemes, we replace the sparsity constraint by an ℓ_1 penalty. We pose the simultaneous estimation of \mathbf{U} and \mathbf{V} from the measurements as the constrained optimization problem

$$\begin{aligned} \{\hat{\mathbf{U}}, \hat{\mathbf{V}}\} = \arg \min_{\mathbf{U}, \mathbf{V}} & \left[\sum_{i=1}^N \|\mathcal{A}_i(\mathbf{U}\mathbf{V}) - \mathbf{b}_i\|_2^2 \right] + \lambda \|\mathbf{U}\|_{\ell_1} \\ & \text{such that } \|\mathbf{V}\|_F^2 \leq c. \end{aligned} \quad (5)$$

The first term in the objective function (5) ensures data consistency. The second term is the sparsity promoting ℓ_1 norm on the entries of \mathbf{U} defined as the absolute sum of its matrix entries: $\mathbf{U} : \|\mathbf{U}\|_{\ell_1} = \sum_{i=1}^M \sum_{j=1}^R |u(i, j)|$. λ is the regularization parameter, and c is a constant that is specified *a priori*. The Frobenius norm constraint on \mathbf{V} is imposed to make the problem well posed; if this constraint is not used, the optimization scheme can end up with coefficients \mathbf{U} that are arbitrarily small in magnitude. While other constraints (e.g., unit norm constraints on

rows) can also be used to make the problem well-posed, the Frobenius norm constraint along with the ℓ_1 sparsity penalty encourages a ranking of temporal basis functions. Specifically, important basis functions are assigned larger amplitudes, while unimportant basis functions are allowed to decay to small amplitudes. We observe that the specific choice of c is not very important; if c is changed, the regularization parameter λ also has to be changed to yield similar results.

D. The Optimization Algorithm

The Lagrangian of the constrained optimization problem in (5) is specified by

$$\mathcal{L}(\mathbf{U}, \mathbf{V}, \eta) = \left[\sum_{i=1}^N \|\mathcal{A}_i(\mathbf{U}\mathbf{V}) - \mathbf{b}_i\|_2^2 \right] + \lambda \|\mathbf{U}\|_{\ell_1} + \eta (\|\mathbf{V}\|_F^2 - c); \quad \eta \geq 0 \quad (6)$$

where η is the Lagrange multiplier.

Since the ℓ_1 penalty on the coefficient matrix is a nondifferentiable function, we approximate it by the differentiable Huber induced penalty which smooths the ℓ_1 penalty

$$\varphi_\beta(\mathbf{U}) = \sum_{i=1}^M \sum_{j=1}^R \psi_\beta(u_{i,j}) \quad (7)$$

where $u_{i,j}$ are the entries of \mathbf{U} and $\psi_\beta(u)$ is defined as

$$\psi_\beta(x) = \begin{cases} |x| - 1/2\beta, & \text{if } |x| \geq \frac{1}{\beta} \\ \beta|x|^2/2, & \text{else.} \end{cases} \quad (8)$$

The Lagrangian function obtained by replacing the ℓ_1 penalty in (6) by φ_β is

$$\mathcal{D}_\beta(\mathbf{U}, \mathbf{V}, \eta) = \left[\sum_{i=1}^N \|\mathcal{A}_i(\mathbf{U}\mathbf{V}) - \mathbf{b}_i\|_2^2 \right] + \lambda \varphi_\beta(\mathbf{U}) + \eta (\|\mathbf{V}\|_F^2 - c); \quad \eta \geq 0. \quad (9)$$

Note that $\varphi_\beta(\mathbf{U})$ is parametrized by the single parameter β . When $\beta \rightarrow \infty$, the Huber induced norm is equivalent to the original ℓ_1 penalty. Other ways to smooth the ℓ_1 norm have been proposed (e.g., [23]).

We observe that the algorithm has slow convergence if we solve for (5) with $\beta \rightarrow \infty$. We use a continuation strategy to improve the convergence speed. Note that the Huber norm simplifies to the Frobenius norm when $\beta = 0$. This formulation (ignoring the constant c and optimization with respect to η) is similar to the one considered in [24]; according to the [24, Lemma 5], the solution of (9) is equivalent to the minimum nuclear norm solution. Here, we assume that the size of the dictionary R is greater than the rank of $\mathbf{\Gamma}$, which holds in most cases of practical interest. Thus, the problem converges to the well-defined nuclear norm solution when $\beta = 0$. Our earlier experiments show that the minimum nuclear norm solution already provides reasonable estimates with reduced aliasing [13]. Thus, the cost function is less vulnerable to local minimum when β is small. Hence, we propose a continuation strategy, where β is initialized to zero and is gradually increased to a large value. By slowly increasing β from zero, we expect to gradually truncate the small coefficients of \mathbf{U} , while relearning the dictionary. Our experi-

ments show that this approach considerably improves the convergence rate and avoids local minima issues.

We rely on the majorize–minimize framework to realize a fast algorithm. We start by majorizing the Huber norm in (9) as² [25]

$$\varphi_\beta(\mathbf{U}) = \min_{\mathbf{L}} \frac{\beta}{2} \|\mathbf{U} - \mathbf{L}\|_F^2 + \|\mathbf{L}\|_{\ell_1} \quad (10)$$

where \mathbf{L} is an auxiliary variable. Substituting (10) in (9), we obtain the following modified Lagrange function, which is a function of four variables: \mathbf{U} , \mathbf{V} , \mathbf{L} , and η

$$\mathcal{D}(\mathbf{U}, \mathbf{V}, \mathbf{L}, \eta) = \sum_{i=1}^N \left[\|\mathcal{A}_i(\mathbf{U}\mathbf{V}) - \mathbf{b}_i\|_2^2 \right] + \eta (\|\mathbf{V}\|_F^2 - c) + \lambda \left[\|\mathbf{L}\|_{\ell_1} + \frac{\beta}{2} \|\mathbf{U} - \mathbf{L}\|_F^2 \right]. \quad (11)$$

The above criterion is dependent on \mathbf{U} , \mathbf{V} , \mathbf{L} , and η and hence have to be solved for all of these variables. While this formulation may appear more complex than the original BCS scheme (5), this results in a simple algorithm. Specifically, we use an alternating minimization scheme to solve (11). At each step, we solve for a specific variable, assuming the other variables to be fixed; we systematically cycle through these subproblems until convergence. The subproblems are specified below

$$\mathbf{L}_{n+1} = \arg \min_{\mathbf{L}} \|\mathbf{U}_n - \mathbf{L}\|_2^2 + \frac{2}{\beta} \|\mathbf{L}\|_{\ell_1} \quad (12)$$

$$\mathbf{U}_{n+1} = \arg \min_{\mathbf{U}} \sum_{i=1}^N \left[\|\mathcal{A}_i(\mathbf{U}\mathbf{V}_n) - \mathbf{b}_i\|_2^2 \right] + \frac{\lambda\beta}{2} \|\mathbf{U} - \mathbf{L}_{n+1}\|_2^2 \quad (13)$$

$$\mathbf{V}_{n+1} = \arg \min_{\mathbf{V}} \sum_{i=1}^N \left[\|\mathcal{A}_i(\mathbf{U}_{n+1}\mathbf{V}) - \mathbf{b}_i\|_2^2 \right] + \eta_n (\|\mathbf{V}\|_F^2 - c). \quad (14)$$

We use a steepest ascent rule to update the Lagrange multiplier at each iteration

$$\eta_{n+1} = (\eta_n + \|\mathbf{V}_{n+1}\|_F^2 - c)_+ \quad (15)$$

where “+” represents the operator defined as $(\tau)_+ = \max\{0, \tau\}$, which is used to ensure the positivity constraint on η [see (9)].

Each of the subproblems are relatively simple and can be solved efficiently, either using analytical schemes or simple optimization strategies. Specifically, (12) can be solved analytically as

$$\mathbf{L}_{n+1} = \frac{\mathbf{U}_n}{\|\mathbf{U}_n\|} \left(\|\mathbf{U}_n\| - \frac{1}{\beta} \right)_+. \quad (16)$$

Since the problems in (13) and (14) are quadratic, we solve it using conjugate gradient (CG) algorithms.

²Note that the right-hand side of (10) is only guaranteed to majorize the Huber penalty $\varphi_\beta(\mathbf{U})$; it does not majorize the ℓ_1 norm of \mathbf{U} ; (as from (8) that $\psi_\beta(x)$ is lower than the ℓ_1 penalty by $1/2\beta$ when $|x| > 1/\beta$. Similarly $\psi_\beta < |x|/2$ when $|x| < 1/\beta$). This majorization in (10) later enables us to exploit simple shrinkage strategies that exist for the ℓ_1 norm; if the ℓ_1 penalty was used instead of the Huber penalty, it would have resulted in more complex expressions than in (16). For additional details, we refer the interested reader to [25].

Once $\|\mathbf{V}\|_F^2 \approx c$, we see that η stabilizes. Hence, we expect (14) to converge quickly. In contrast, the condition number of the \mathbf{U} subproblem is dependent on β . Hence, the convergence of the algorithm will be slow at high values of β . In addition, the algorithm may converge to a local minimum if it is initialized directly with a large value of β . We use the above mentioned continuation approach to solve for simpler problems initially and progressively increase the complexity. Specifically, starting with an initialization of \mathbf{V} , the algorithm iterates between (12) and (15) in an inner loop, while progressively updating β starting with a small value in an outer loop. The inner loop is terminated when the cost in (6) stagnates. The outer loop is terminated when a large enough β is achieved. We define convergence as when the cost in (6) in the outer loop stagnates to a threshold of 10^{-5} . In general, with our experiments on dynamic MRI data, we observed convergence when the final value of β is approximately 10^{13} to 10^{15} times larger than the initial value of β .

III. EXPERIMENTAL EVALUATION

We describe in Sections III-A and III-B the algorithmic considerations of the proposed BCS framework. We then perform phase transition experiments using numerical phantoms to empirically demonstrate the uniqueness of the BCS framework (Section III-C). We finally compare the reconstructions of BCS against existing low rank and compressed sensing schemes using *in vivo* Cartesian and radial free breathing myocardial perfusion MRI datasets (Section III-D).

A. Comparison of Different BCS Schemes

In this section, we compare the performance of the proposed scheme with two other potential BCS implementations. Specifically, we focus on the rate of convergence and the sensitivity to initial guesses of the following schemes.

- **Proposed BCS:** The proposed BCS formulation specified by (5) solved by optimizing \mathbf{U} and \mathbf{V} using the proposed majorize–minimize algorithm; the algorithm cycles through steps specified by (12)–(15).
- **Alternating BCS:** The proposed BCS formulation specified by (5) solved by alternatively optimizing for the sparse coefficients \mathbf{U} and the dictionary \mathbf{V} . Specifically, the sparse coding step (solving for \mathbf{U} , assuming a fixed \mathbf{V}) is performed using the state of the art augmented Lagrangian optimization algorithm [26]. The dictionary learning subproblem solves for \mathbf{V} , assuming \mathbf{U} to be fixed. This is solved by iterating between a quadratic subproblem in \mathbf{V} (solved by a conjugate gradient algorithm), and a steepest ascent update rule for η [similar to (15)]. The update of η ensures the Frobenius norm constraint on \mathbf{V} is satisfied at the end of the \mathbf{V} subproblem. Both of the sparse coding and dictionary learning steps are iterated until convergence.
- **Greedy BCS:** We adapt the extension of the K-SVD scheme that was used for patch based 2-D image recovery [20] to our setting of dynamic imaging. This scheme models the rows of $\mathbf{\Gamma}$ in the synthesis dictionary with

temporal basis functions [as in (4)]. Specifically, it solves the following optimization problem:

$$\{\hat{\mathbf{\Gamma}}, \hat{\mathbf{U}}, \hat{\mathbf{V}}\} = \arg \min_{\mathbf{\Gamma}, \mathbf{U}, \mathbf{V}} \|\mathbf{\Gamma} - \mathbf{U}\mathbf{V}\|_2^2; \text{ such that}$$

$$\sum_{i=1}^N \|\mathcal{A}_i(\mathbf{\Gamma}) - \mathbf{b}_i\|_2^2 < \sigma_n$$

$$\|\mathbf{u}_k\|_0 \leq j; \quad k = 1, \dots, M$$

$$\|\mathbf{v}_q\|_2^2 = 1; \quad q = 1, \dots, R \quad (17)$$

where σ_n is the standard deviation of the measurement noise. Here the ℓ_0 norm is used to impose the sparsity constraints on the rows (indexed by k) of \mathbf{U} . The number of nonzero coefficients (or the sparsity level) of each row of \mathbf{U} is given by j . The unit column norm constraints are used on the elements of the dictionary to ensure well posedness (avoid scaling ambiguity). Starting with an initial estimate of the image data given by the zero filled inverse Fourier reconstruction $\mathbf{\Gamma}_{\text{init}}$, the BCS scheme in this setting iterates between a denoising/dealiasing step to update \mathbf{U} , \mathbf{V} , and an image reconstruction step to update $\mathbf{\Gamma}$. The denoising step involves dictionary learning and sparse coding with ℓ_0 minimization. It utilizes the K-SVD algorithm [19] which takes a greedy approach to update \mathbf{U} and \mathbf{V} . We implemented the K-SVD algorithm based on the codes available at the authors webpage [27]. The K-SVD implementation available online was modified to produce complex dictionaries. For sparse coding, we used the orthogonal matching pursuit algorithm (OMP). We used the approximation error threshold along with the sparsity threshold (upper bound on j) in OMP. The approximation error threshold was set to 10^{-6} . Our implementation also considered the pruning step described in [19] and [21] to minimize local minima effects. Specifically, if similar basis functions were learnt, one of them was replaced with the voxel time profile that was least represented. In addition, if a basis function was not being used enough, it was replaced with the voxel time profile that was least represented. Other empirical heuristics such as varying the approximation error threshold in the OMP algorithm during the different iteration (alteration) steps may also be considered in the greedy BCS scheme. In this work, we restrict ourselves to a fixed error threshold of 10^{-6} due to the difficulty of tuning for an optimal set of different error threshold values for different alteration steps.

In Fig. 2, we aim to recover a myocardial perfusion MRI dataset with considerable interframe motion ($N_x \times N_y \times N_t = 190 \times 90 \times 70$) from its undersampled $k - t$ measurements using the above three BCS schemes. We considered a noiseless simulation in this experiment for all the three BCS schemes. While resampling, we used a radial trajectory with 12 uniformly spaced rays within a frame with subsequent random rotations across frames to achieve incoherency. This corresponded to an

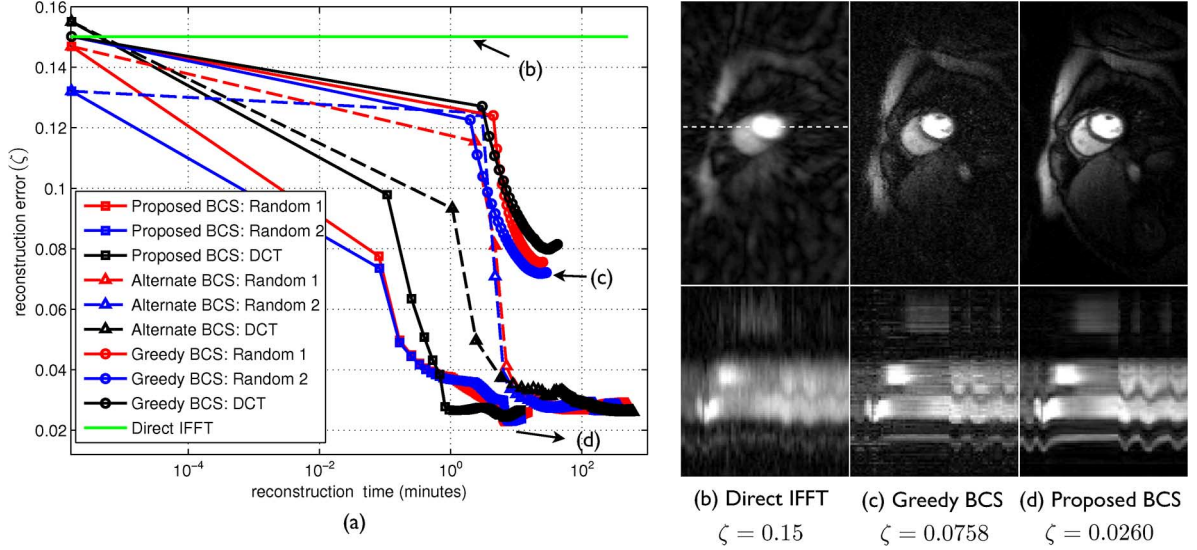


Fig. 2. Comparison of different BCS schemes: In (a), we show the reconstruction error vs reconstruction time for the proposed BCS, alternate BCS, and the greedy BCS schemes. The free parameters of all the schemes were optimized to yield the lowest possible errors, while the dictionary sizes of all methods were fixed to 45 atoms. We plot the reconstruction error as a function of the CPU run time for the different schemes with different dictionary initializations. The proposed BCS and alternating BCS scheme converged to the same solution irrespective of the initialization. However, the proposed scheme is observed to be considerably faster; note that the alternating scheme takes around ten times more time to converge. It is also seen that the greedy BCS scheme converged to different solutions with different initializations, indicating the dependence of these schemes on local minima.

acceleration of 7.5 fold. We used 45 basis functions in the dictionary. We compare the performance of the different BCS algorithms with different initializations of the dictionary \mathbf{V} . Specifically, we used dictionaries with random entries, and a dictionary with the discrete cosine transform (DCT) bases. To ensure fair comparisons, we optimized the parameters of all the three schemes: (i.e., regularization parameter λ in the proposed and alternating BCS schemes, as well as the sparsity level j in the greedy BCS scheme). These were chosen such that the normalized error between the reconstruction and the fully sampled data was minimal. A sparsity level of $j = 3$ was found to be optimal for the greedy BCS scheme. Further, in the greedy BCS scheme, after the first iteration, we initialized the K-SVD algorithm with the dictionary obtained from the previous iteration. We used the same stopping criterion in both the proposed and alternate BCS schemes: the iterations were terminated when the cost in (6) stagnated to a threshold of 10^{-5} . All the algorithms were run on a linux work station with a 4 core Intel Xeon processor and 24 GB RAM.

From Fig. 2, we observe both the proposed and alternate BCS schemes to be robust to the choice of initial guess of the dictionary. They converged to almost the same solution with different initial guesses. However, the proposed BCS scheme converged to the solution significantly faster (at least by a factor of 10 fold) compared to the alternate BCS scheme. From Fig. 2, we observe the number of iterations for both the proposed and the alternate BCS schemes to be similar. However, since the alternate BCS scheme solves for the sparse ℓ_1 minimization problem fully during each iteration, it is more expensive than the proposed BCS scheme. On an average, an iteration of the alternate BCS scheme was ≈ 10 slower than an iteration of the proposed BCS scheme. From Fig. 2, we note the greedy BCS scheme to converge to different solutions for different initial guesses. Additionally, as noted in Fig. 2(c) and (d), the reconstructions with

the proposed BCS scheme were better than the reconstructions with the greedy BCS scheme. Although the temporal dynamics were faithfully captured in the greedy BCS reconstructions, it suffered from noisy artifacts. This was due to modeling with noisy basis functions, which were learned by the algorithm from under sampled data (see Fig. 3). Note that this scheme uses the unit column norm constraints which has all the basis functions are ranked equally. In contrast, since the proposed scheme uses the ℓ_1 sparsity penalty and the Frobenius norm dictionary constraint, the energy of the learned bases functions varied considerably (see Fig. 3). With the proposed scheme, the ℓ_1 minimization optimization ensures that the important basis functions (basis functions that are shared by several voxels) will have a higher energy. Similarly, the unimportant noise-like basis functions that play active roles in fewer voxels will be attenuated, since the corresponding increase in $\|\mathbf{U}\|_{\ell_1}$ is small. Thus, the ℓ_1 penalty-Frobenius norm combination results in a model order selection, which is more desirable than the ℓ_0 penalty-column norm combination. This choice is especially beneficial in the undersampled case since the number of basis functions that can be reliably recovered is dependent on the number of measurements and the signal to noise ratio.

B. Choice of Parameters

The performance of the BCS scheme depends on the choice of two parameters: regularization parameter λ and the number of bases in the dictionary R . Even though the criterion in (5) depends on c , varying it results in a renormalization of the dictionary elements and hence changing the value of λ . We set the value of c as 800 for both the numerical and *in vivo* experiments. We now discuss the behavior of the BCS model with respect to changes in λ and R .

1) *Dependence on λ* : We observe that if a low λ is used, the model coefficient matrix \mathbf{U} is less sparse. This results in

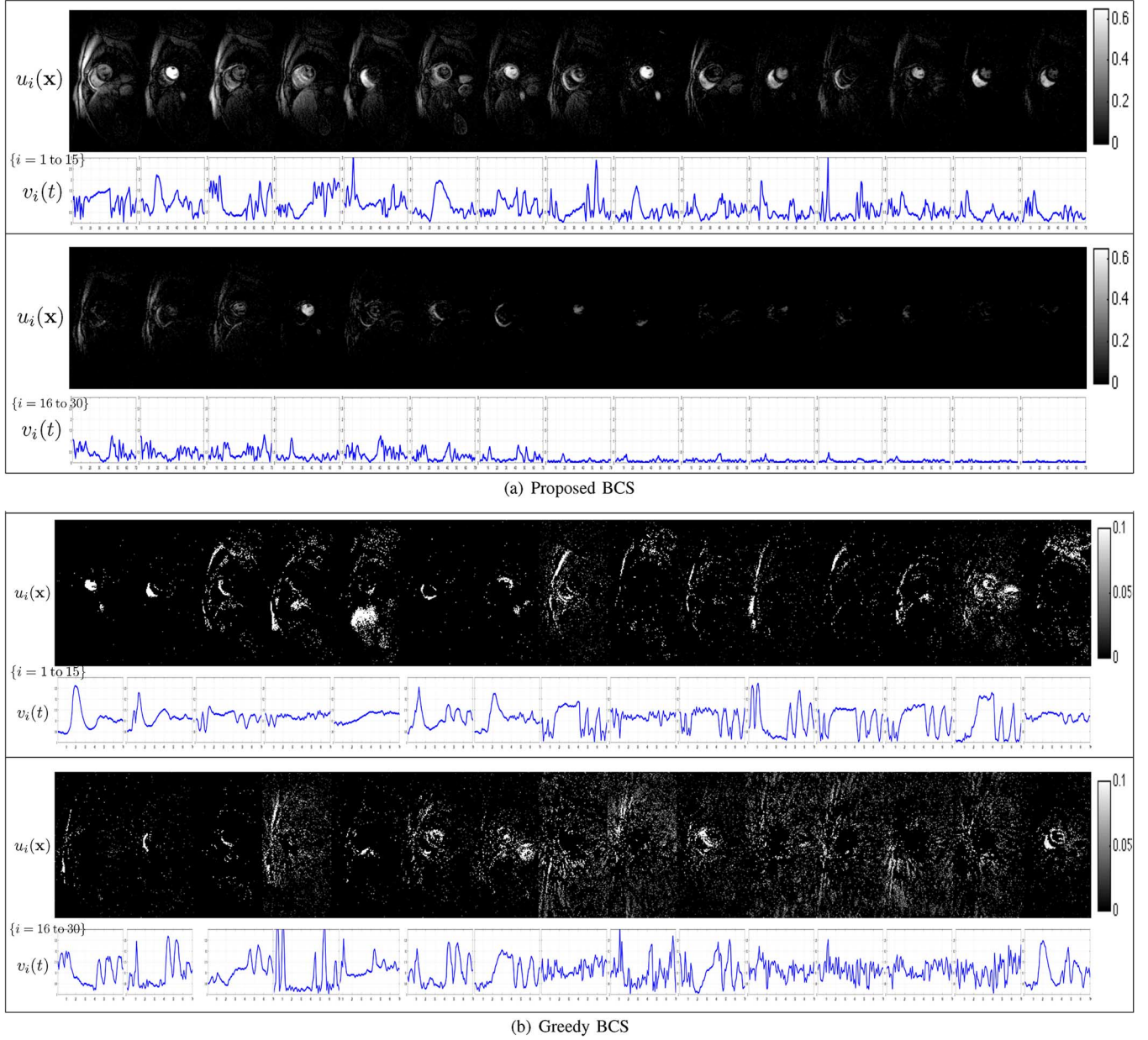


Fig. 3. Model coefficients and dictionary bases. We show few of the estimated spatial coefficients $u_i(\mathbf{x})$ and its corresponding temporal bases $v_i(t)$ from 7.5 fold undersampled myocardial perfusion MRI data (data in Fig. 2). (a) Corresponds to the estimates using the proposed BCS scheme, while (b) is estimated using the greedy BCS scheme. For consistent visualization, we sort the product entries $u_i(\mathbf{x})v_i(t)$ according to their ℓ_2 norm, and show the first 30 sorted terms. Note that the BCS basis functions are drastically different from exponential basis functions in the Fourier dictionary; they represent temporal characteristics specific to the dataset. It can also be seen that the energy of the basis functions in (a) varies considerably, depending on their relative importance. Since we rely on the ℓ_1 sparsity norm and Frobenius norm dictionary constraint, the representation will adjust the scaling of the dictionary basis functions $v_i(t)$ such that the $\|\mathbf{U}\|_{\ell_1}$ is minimized. Specifically, the ℓ_1 minimization optimization will ensure that basis functions used more frequently are assigned higher energies, while the less significant basis functions are assigned lower energy [see $v_{25}(t)$ to $v_{30}(t)$], hence providing an implicit model order selection. By contrast, the formulation of the greedy BCS scheme involves the setting of ℓ_0 sparsity norm and column norm dictionary constraint; the penalty is only dependent on the sparsity of \mathbf{U} . Unlike the proposed scheme, this does not provide an implicit model order selection, resulting in the preservation of noisy basis functions, whose coefficients capture the alias artifacts in the data. This explains the higher errors in the greedy BCS reconstructions in Fig. 2.

representing each voxel profile using many temporal basis functions. Since the number of degrees-of-freedom on the scheme depends on the number of sparse coefficients, this approach often results in residual aliasing in datasets with large motion. In contrast, heavy regularization results in modeling the entire dynamic variations in the dataset using very few temporal basis functions; this often results in temporal blurring and loss of temporal detail. In the experiments in this paper, we have access to

the fully sampled ground truth data. As depicted in Fig. 4(a), we choose the optimal λ such that the error between the reconstructions and the fully sampled ground truth data, specified by

$$\zeta = \left(\frac{\|\mathbf{\Gamma}_{\text{recon}} - \mathbf{\Gamma}_{\text{orig}}\|_F^2}{\|\mathbf{\Gamma}_{\text{orig}}\|_F^2} \right) \quad (18)$$

is minimized. Furthermore, *in vivo* experiments with myocardial perfusion MRI datasets, we optimize λ by evaluating the

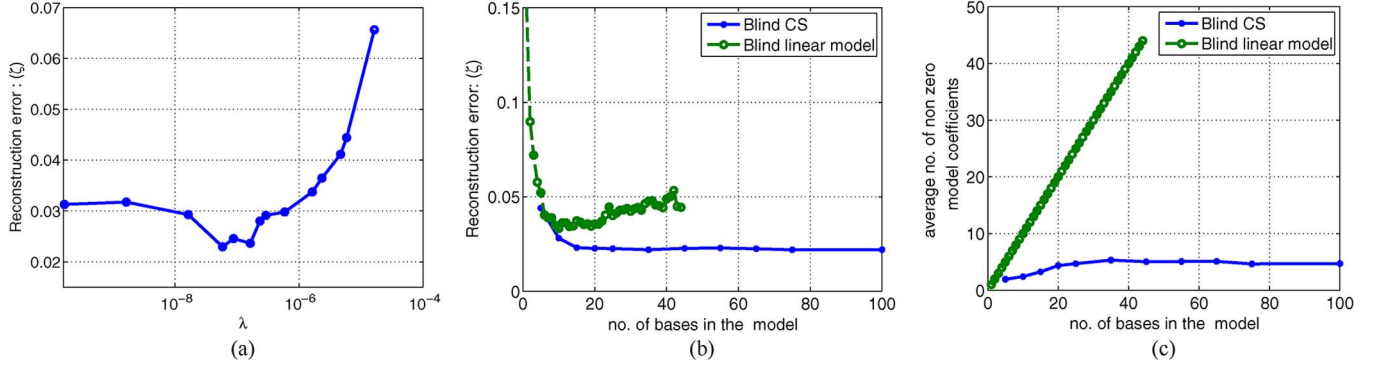


Fig. 4. BCS model dependence on the regularization parameter and the dictionary size: (a) shows the reconstruction error (ζ) as a function of different λ in the BCS model. The plots in (b) and (c), respectively, show the reconstruction error (ζ) and the average number of nonzero model coefficients of the BCS and the BLM schemes as a function of the number of bases in the respective models. As depicted in (a), we optimize our choice of λ such that the error between the fully sampled data and the reconstruction is minimal. From (b), we observe that the BCS reconstruction error reduces with the dictionary size and hits a plateau after a size of 20 basis functions. This is in sharp contrast with the BLM scheme where the reconstructions errors increase when the basis functions are increased. The average number of BCS model coefficients unlike the BLM has a nonlinear relation with the dictionary size reaching saturation to a number of 4–4.5. The plots in (b) and (c) depict that the BCS scheme is insensitive to dictionary size as long as a reasonable size (at least 20 in this case) is chosen. We chose a dictionary size of 45 bases in the experiments considered in this paper.

reconstruction error only in a field of view that contained regions of the heart (ζ_{ROI} , ROI: region of interest), specified by

$$\zeta_{\text{ROI}} = \left(\frac{\|\mathbf{\Gamma}_{\text{recon,ROI}} - \mathbf{\Gamma}_{\text{orig,ROI}}\|_F^2}{\|\mathbf{\Gamma}_{\text{orig,ROI}}\|_F^2} \right). \quad (19)$$

This metric is motivated by recent findings in [28], and by our own experience in determining a quantitative metric that best describes the accuracy in reproducing the perfusion dynamics in different regions of the heart, and the visual quality in terms of minimizing visual artifacts, and preserving crispness of borders of heart.

We realize that the above approach of choosing the regularization parameter is not feasible in practical applications, where the fully sampled reference data is not available. In these cases, one can rely on simply heuristics such as the L-curve strategy [29], or more sophisticated approaches for choosing the regularization parameters [30], [31]. The discussion of these approaches in this context are beyond the scope of this paper.

2) *Dependence on the Dictionary Size:* In Fig. 4(b) and (c), we study the behavior of the BCS model as the number of basis functions in the model increase. We perform BCS reconstructions using dictionary sizes ranging from 5 to 100 temporal bases. The plot the reconstruction errors and the average number of nonzero model coefficients³ as a function of the number of basis functions are shown in Fig. 4(b) and (c), respectively. We observe that the BCS reconstructions are insensitive to the dictionary size beyond 20–25 basis functions. We attribute the insensitivity to number of basis functions to the combination of the ℓ_1 sparsity norm and the Frobenius norm constraint on the dictionary (see Fig. 3). Note that the number of basis functions that can be reliably estimated from under sampled data is limited by the number of measurements and the signal to noise ratio, unlike the classical dictionary learning setting where extensive

training data is available. As discussed earlier (Section III-A), the ℓ_1 sparsity norm and the Frobenius norm dictionary constraint allows the energy of the basis functions to be considerably different. Hence, the optimization scheme ranks the basis functions in terms of their energy, allowing the insignificant basis functions (which models the alias artifacts and noise) to decay to very small amplitudes. Based on these above observations, we fix the BCS dictionary size to 45 basis functions in the rest of the paper. Note that since $45 < 70 =$ the number of time frames of the data, this is an undercomplete representation. From Fig. 4(c), we observe that the average number of nonzero model coefficients to be approximately constant (≈ 4 –4.5) for dictionary sizes greater than 20 bases. The BCS model is also compared to the blind linear model (low-rank representation) in Fig. 4(b) and (c). The number of nonzero model coefficients in the blind linear model grows linearly with the number of bases. This implies that the temporal bases modeling error artifacts and noise are also learned as the number of basis functions increase. This explains the higher reconstruction errors observed with the blind linear models as the number of basis functions increase beyond a limit.

C. Numerical Simulations

To study the uniqueness of the proposed BCS formulation in (5), we evaluate the phase transition behavior of the algorithm on numerical phantoms. We generate dynamic phantoms with varying sparsity levels by performing dictionary learning on a fully sampled myocardial perfusion MRI dataset with motion ($N_x \times N_y \times N_t = 190 \times 90 \times 70$); i.e., $M = 17100$; $N = 70$. We use the K-SVD algorithm [19] to approximate the fully sampled Casorati matrix $\mathbf{\Gamma}_{M \times N}$ as a product of a sparse coefficient matrix $\mathbf{U}_{M \times R}^j$ and a learned dictionary $\mathbf{V}_{R \times N}^j$ by solving

$$\begin{aligned} \{\hat{\mathbf{U}}^j, \hat{\mathbf{V}}^j\} &= \arg \min_{\mathbf{U}^j, \mathbf{V}^j} \|\mathbf{\Gamma} - \mathbf{U}^j \mathbf{V}^j\|_F^2 \\ \text{s.t. } \quad &\|\mathbf{u}_i\|_0 \leq j; \quad i = 1, 2, \dots, M \\ &\|\mathbf{v}_q\|_2 = 1; \quad q = 1, \dots, R. \end{aligned} \quad (20)$$

³Evaluated by performing the average of the number of nonzero coefficients in the rows of the matrix $\mathbf{U}_{M \times R}$ that was thresholded at 1% of the maximum value of \mathbf{U} .

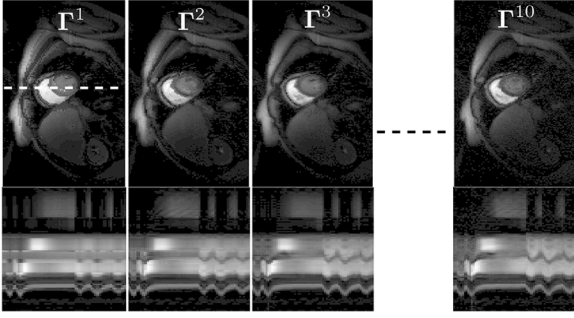


Fig. 5. Numerical phantoms Γ^j , which are used in the simulation study in Fig. 6. Here j is the number of nonzero coefficients (sparsity levels) at each pixel. The top and bottom rows respectively show one spatial frame and the image time profile through the dotted white line. Note that the sparse decomposition provides considerable temporal detail even for a sparsity of one. This is possible since different temporal basis functions are active at each pixel.

Here, j denotes the number of nonzero coefficients in each row of \mathbf{U}^j . We set the size of the dictionary as $R = 45$. We construct different dynamic phantoms corresponding to different values of j ranging from ($j = 1, 2, \dots, 10$) as $\Gamma^j = \mathbf{U}^j \mathbf{V}^j$. Few of these phantoms are shown in Fig. 5. Note that the K-SVD model is somewhat inconsistent with our formulation since it relies on ℓ_0 penalty and uses the unit column norm constraint, compared to the ℓ_1 penalty and Frobenius norm constraint on the dictionary in our setting.

We perform experiments to reconstruct the spatio-temporal datasets Γ^j from $k - t$ measurements that are undersampled at different acceleration factors. Specifically, we employ a radial sampling trajectory with “ l ” number of uniformly spaced rays within a frame with subsequent random rotations across time frames; the random rotations ensure incoherent sampling. We consider different number of radial rays ranging from $l = 4, 8, 12, \dots, 56$ to simulate undersampling at different acceleration rates. The reconstructions were performed with three different schemes.

- 1) Classical compressed sensing method, where the signal is assumed to be sparse in the temporal Fourier domain (CS) [5].
- 2) The proposed BCS method, where the sparse coefficients and the dictionary are estimated from the measurements.
- 3) Dictionary aware CS: this approach is similar to 1, except that the dictionary \mathbf{V}^j is assumed to be known. This case is included as an upper-limit for achievable acceleration.

The performance of the above schemes were compared by evaluating the normalized reconstruction error metric ζ (18). All the above reconstruction schemes were optimized for their best performance by tuning the regularization parameters such that ζ was minimal.

The phase transition plots of the reconstruction schemes are shown in Fig. 6. We observe that the CS scheme using Fourier dictionary result in poor recovery rates in comparison to the other schemes. This is expected since the myocardial perfusion data is not sparse in the Fourier basis. As expected, the dictionary aware case (the exact dictionary in which the signal is sparse is prespecified) provides the best results. However, we observe that the performance of the BCS scheme is only marginally worse than the dictionary aware scheme. As explained

before, most of the degrees-of-freedom in the BCS representation is associated with the sparse coefficients. By contrast, the number of free parameters associated with the dictionary is comparatively far smaller since the number of voxels is far greater than the number of time frames. This clearly shows that the overhead in additionally estimating the dictionary is minimal in the dynamic imaging scenario. This property makes the proposed scheme readily applicable and very useful in dynamic imaging applications (e.g., myocardial perfusion, free breathing cine), where the signal is not sparse in pre-specified dictionaries.

D. Experiments on in vivo Datasets

1) *Data Acquisition and Undersampling:* We evaluate the performance of the BCS scheme by performing retrospective undersampling experiments on contrast enhanced dynamic MRI data. We consider one brain perfusion MRI dataset acquired using Cartesian sampling, and two free breathing myocardial perfusion MRI datasets that were acquired using Cartesian sampling, and radial sampling, respectively.

The myocardial perfusion MRI datasets were obtained from subjects scanned on a Siemens 3T MRI at the University of Utah in accordance to the institute’s review board. The Cartesian dataset was acquired under rest conditions after a Gd bolus of 0.02 mmol/kg. The radial dataset was acquired under stress conditions where 0.03 mmol/kg of Gd contrast agent was injected after 3 min of adenosine infusion. The Cartesian dataset (phase \times frequency encodes \times time = $90 \times 190 \times 70$) was acquired using a saturation recovery FLASH sequence (three slices, TR/TE = 2.5/1.5 ms, sat. recovery time = 100 ms). The motion in the data was due to improper gating and/or breathing; [see the ripples in the time profile in Fig. 7(c)]. The radial data was acquired with a perfusion radial FLASH saturation recovery sequence (TR/TE 2.5/1.3 ms). 72 radial rays equally spaced over π radians and with 256 samples per ray were acquired for a given time frame. The rays in successive frames were rotated by a uniform angle of $\pi/288$ radians, which corresponds to a period of 4 across time. The acquired radial data corresponds to an acceleration factor of ≈ 3 compared to Nyquist. Since this dataset is slightly under sampled, we use a spatio-temporal total variation (TV) constrained reconstruction algorithm to generate the reference data in this case. We observe that this approach is capable of resolving the slight residual aliasing in the acquired data.

The single slice brain perfusion MRI dataset was obtained from a multi slice 2-D dynamic contrast enhanced (DCE) patient scan at the University of Rochester. The patient had regions of tumor identified in the DCE study. The data corresponded to 60 time frames separated by TR = 2 s; the matrix size was $128 \times 128 \times 60$.

Retrospective downsampling experiments were done using two different sampling schemes respectively for the Cartesian and radial acquisitions. Specifically, the Cartesian datasets were resampled using a radial trajectory with 12 uniformly spaced rays within a frame with subsequent random rotations across frames to achieve incoherency. This corresponds to a net acceleration level of 7.5 in the cardiac data, and 10.66 in the brain data. Retrospective undersampling of the cardiac radial data was done by considering 24 rays from the acquired 72 ray dataset.

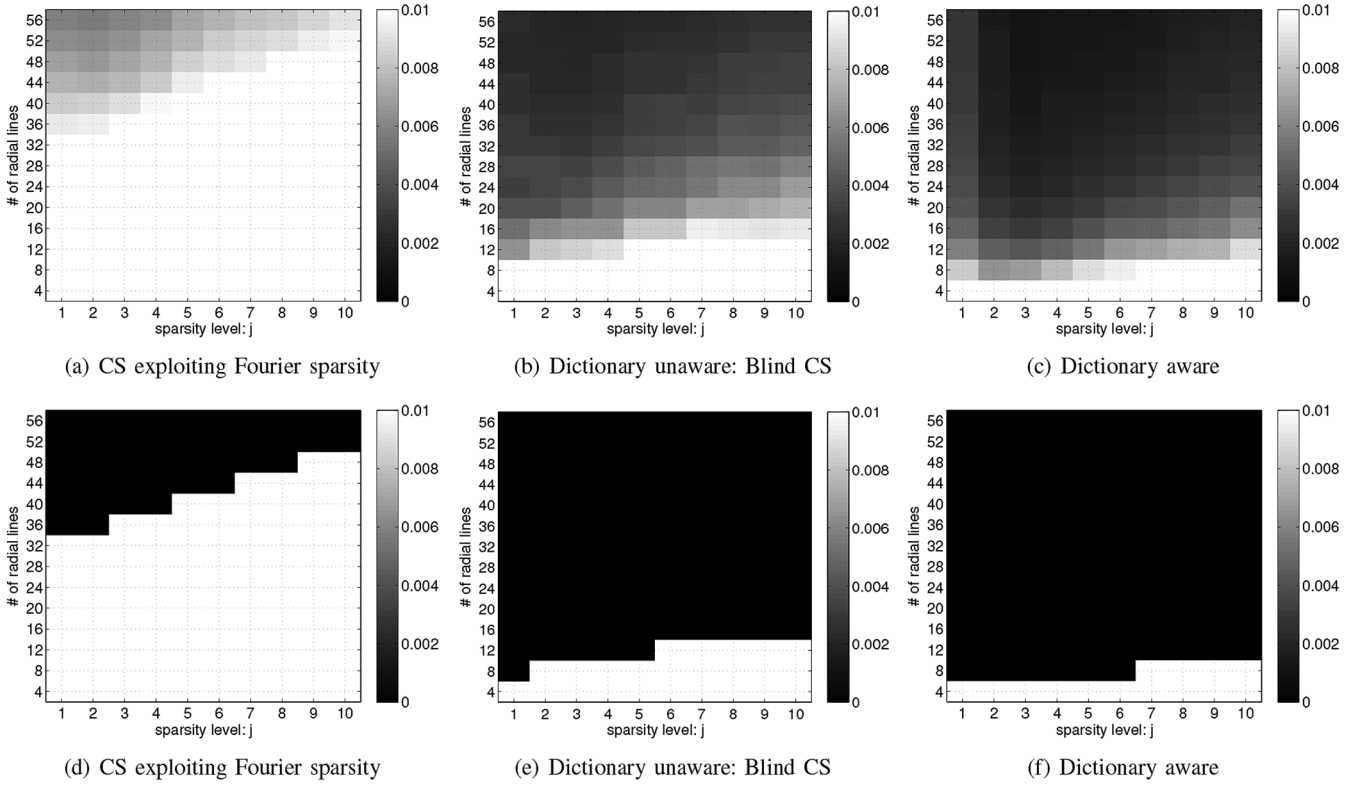


Fig. 6. Phase transition behavior of various reconstruction schemes: Top row: Normalized reconstruction error ζ is shown at different acceleration factors (or equivalently different number of radial rays in each frame) for different values of j . Bottom row: ζ thresholded at 1% error; black represents 100% recovery. We study the ability of the algorithms to reliably recover each of the data sets Γ^j from different number of radial samples in k-space. The Γ^j , shown in Fig. 5 are the j sparse approximations of a myocardial perfusion MRI dataset with motion. As expected, the number of lines required to recover the dataset increases with the sparsity. The BCS scheme outperformed the compressed sensing scheme considerably. The learned dictionary aware scheme yielded the best recovery rates. However, due to a small overhead in estimating the dictionary, the dictionary unaware (BCS) scheme was only marginally worse than the dictionary aware scheme.

These rays were chosen such that they were approximately separated by the golden angle distance ($\pi/1.818$). The golden angle distribution ensured incoherent k-t sampling. The acquisition using 24 rays corresponds to an acceleration of ≈ 10.6 fold when compared to Nyquist. This acceleration can be capitalized to improve many factors in the scan (e.g., increase the number of slices, improve the spatial resolution, improve quality in short duration scans such as systolic or ungated imaging).

2) *Evaluation of BCS Against Other Reconstruction Schemes:* We compare the BCS algorithm against the following schemes:

- low rank promoting reconstruction using Schatten p -norm (Sp-N) ($p = 0.1$) minimization [13].
- CS exploiting temporal Fourier sparsity [5]

We compared different low-rank methods including two step low rank reconstruction [10], nuclear norm minimization [13], incremented rank power factorization (IRPF) [12], and observed that the Schatten p -norm minimization scheme provides comparable, or even better, results in most cases that we considered [32]. Hence, we chose the Schatten p -norm reconstruction scheme in our comparisons. For a quantitative comparison amongst all the methods, we use the normalized reconstruction error metrics defined in (18), (19) and the high-frequency normalized error norm metric (HFEN). The HFEN metric was used

in [20] to quantify the quality of fine features, and the edges in the images, and is defined as

$$\text{HFEN} = \frac{1}{N} \sum_{i=1}^N \frac{\|\text{LoG}(\mathbf{\Gamma}_{\text{recon},i}) - \text{LoG}(\mathbf{\Gamma}_{\text{ideal},i})\|_F^2}{\|\text{LoG}(\mathbf{\Gamma}_{\text{ideal},i})\|_F^2} \quad (21)$$

where LoG is a Laplacian of Gaussian filter that capture edges. We use the same filter specifications as in [20]: kernel size of 15×15 pixels, with a standard deviation of 1.5 pixels.

The comparisons on the Cartesian rest myocardial perfusion MRI dataset are shown in Fig. 7. We observe that the frames with significant motion content and contrast variations are considerably blurred with the low rank method. By contrast, the BCS scheme robustly recovers these regions with minimum spatio-temporal blur. The BCS scheme is more robust than the CS scheme. Specifically the former is robust to breathing motion, while the CS scheme results in motion blur (see arrows in Fig. 7 iv.e and iv.f).

Fig. 8 shows the comparisons on the brain perfusion MRI dataset. We observe BCS to retain the subtle details and edges of the various structures in the brain. It shows superior spatio-temporal fidelity. In contrast, the CS and low rank schemes suffer from spatio-temporal blurring artifacts as depicted in Fig. 8.

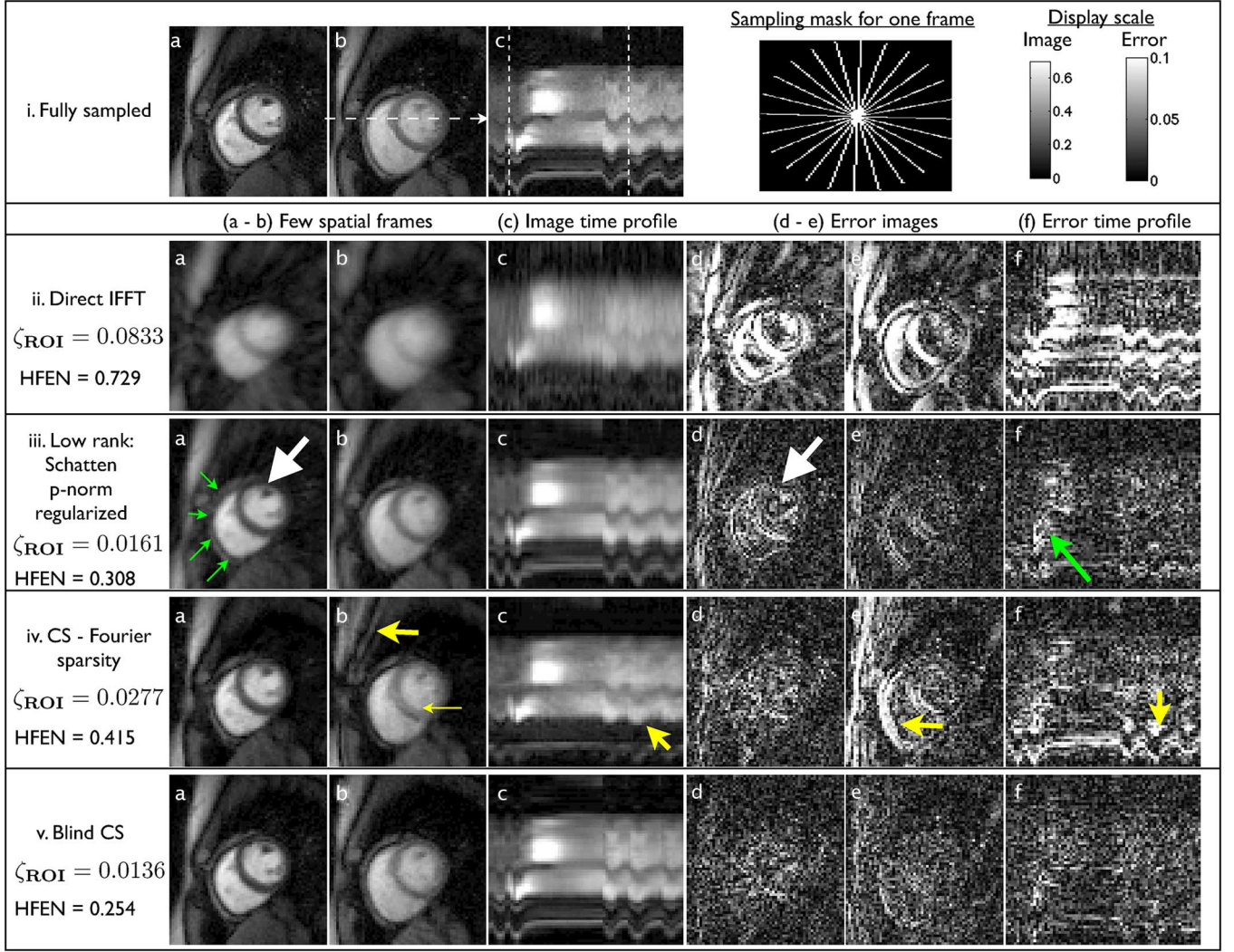


Fig. 7. Comparison of the proposed scheme with different methods on a retrospectively downsampled Cartesian myocardial perfusion data set with motion at 7.5 fold acceleration: A radial trajectory is used for downsampling. The trajectory for one frame is shown in (i). The trajectory is rotated by random shifts in each time frame. Reconstructions using different algorithms, along with the fully sampled data are shown in (i)–(v). (a), (b), (c), (d), (e), (f), respectively, show few spatial frames, image time profile, corresponding error images, error in image time profile. The image time profile in (c) is through the dotted line in (i.b). The ripples in (i.c) correspond to the motion due to inconsistent gating and/or breathing. The location of the spatial frames along time is marked by the dotted lines in (i.c). We observe the BCS scheme to be robust to spatio-temporal blurring, compared to the low rank model; e.g., see the white arrows, where the details of the papillary muscles are blurred in the Schatten p-norm reconstruction while maintained well with BCS. This is depicted in the error images as well, where BCS has diffused errors, while the low rank scheme (iii) have structured errors corresponding to the anatomy of the heart. The BCS scheme was also robust to the compromises observed with the CS scheme; the latter was sensitive to breathing motion as depicted by the arrows in iv.

In Fig. 9, we compare the various reconstruction schemes on the radial data acquired during stress conditions. We observe performance similar to Fig. 7. The low rank reconstructions exhibit reduced temporal fidelity. The reduced fidelity can result in inaccurate characterization of the contrast dynamics uptake. The CS reconstructions have considerable spatio-temporal blur. In particular, the borders of the heart and the papillary muscles are blurred with the CS scheme. By contrast, the BCS scheme provides crisper images and are robust to spatio-temporal blur.

IV. DISCUSSION

We proposed a novel blind compressive sensing framework for accelerating dynamic MRI. Since the dictionary is learned from the measurements, we observe superior reconstructions compared to compressive sensing schemes that assume fixed

dictionaries. Our numerical simulations and phase transition plots show that the overhead in additionally estimating the dictionary is only marginally higher than the case with known dictionary. This observation is valid in the dynamic imaging context since the number of nonzero coefficients (dependent on the number of pixels) is much higher than the size of the dictionary (dependent on the number of time frames).

We have also drawn similarities and important distinctions between the BCS scheme and blind linear models or low-rank methods. Our experiments show superior performance of the BCS scheme in comparison to the blind linear model. Specifically, better temporal fidelity, reduced spatial artifacts, sharper spatial features were distinctly observed with BCS when compared to blind linear model. These improvements can be attributed to the richness of the model in having an overcomplete set of learned temporal bases.

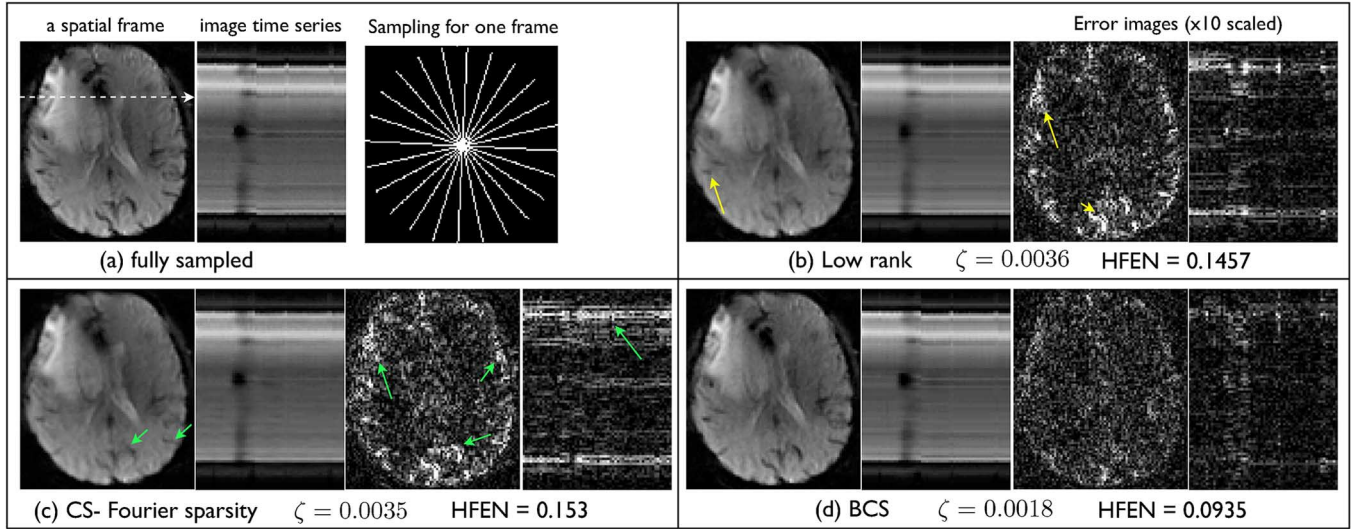


Fig. 8. Comparisons of the different reconstructions schemes on a brain perfusion MRI dataset. The fully sampled data in (a) is retrospectively undersampled at a high acceleration of 10.66. The radial sampling mask for one frame is shown in (a), subsequent frames had the mask rotated by random angles. We show a spatial frame, the image time series, and the corresponding error images for all the reconstruction schemes. Note from (b) and (c), the low rank and CS schemes have artifacts in the form of spatiotemporal blur; the various fine features are blurred (see arrows). In contrast, the BCS scheme had crisper features, and superior spatiotemporal fidelity. The reconstruction error and the HFEN error numbers were also considerably less with the BCS scheme.

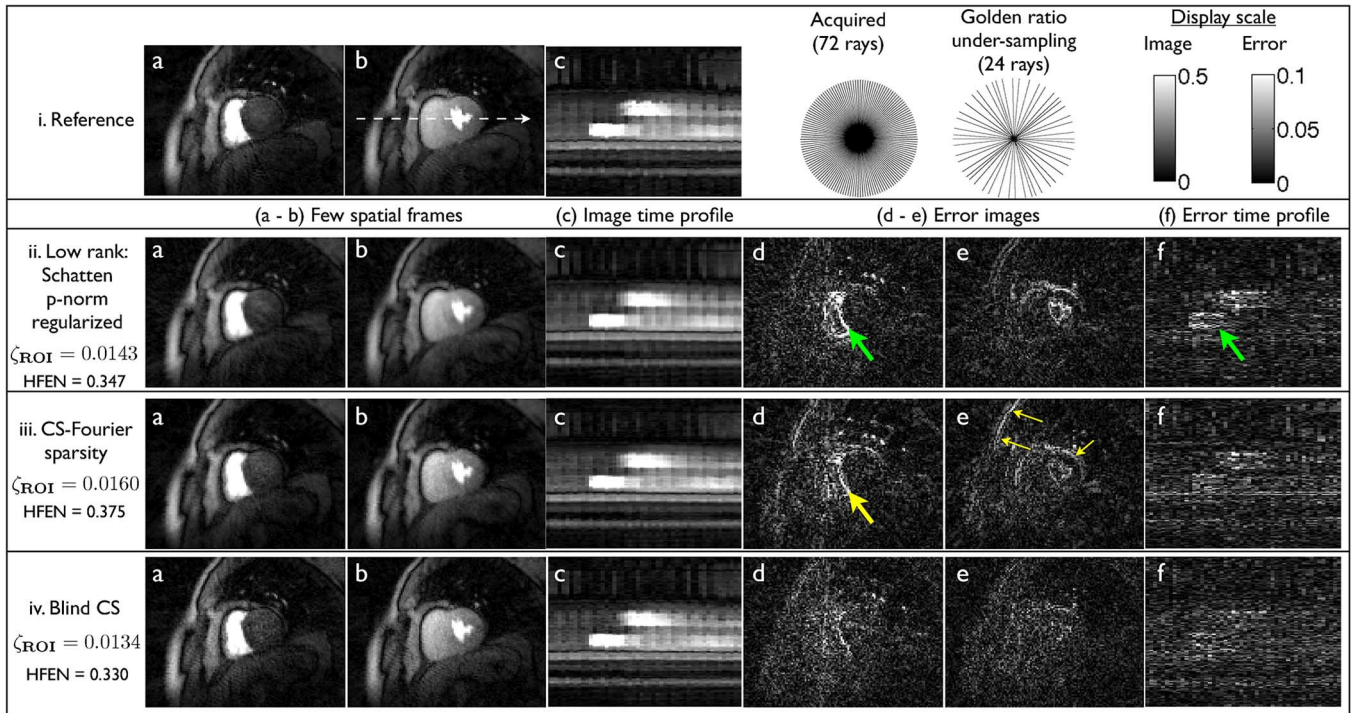


Fig. 9. Comparisons of different reconstruction schemes on a stress myocardial perfusion MRI dataset with breathing motion: Retrospective sampling was considered by picking 24 radial rays/frame from the acquired 72 ray data; the rays closest to the golden ratio pattern was chosen. Few spatial frames, the corresponding image time profile, error frames, and error in image time profile are shown for all the schemes. We specifically observe loss of important borders and temporal blur with the low rank and CS schemes while the BCS reconstructions have crisper borders and better temporal fidelity. Also note from the columns (d)–(f) that the errors in the BCS scheme are less concentrated at the edges, compared to the other methods. This indicates that the edge details and temporal dynamics are better preserved in the BCS reconstructions.

The proposed setting is fundamentally different from approaches that use dictionaries learnt from exemplar data and use them to recover similar images. The proposed setting learns the dictionaries jointly with the reconstruction directly from undersampled data. We observe the learnt temporal basis functions to be heavily dependent on respiration patterns, cardiac

rate, timing of the bolus, gadolinium dosage, adenosine dosage, and the arterial input function (see Fig. 3). Since these patterns would vary from subject to subject, the dictionaries learnt from the data at hand would be more beneficial in capturing subject specific patterns than dictionaries learnt from a data base of images.

The comparison of the proposed algorithm against an alternating scheme to minimize the same cost function, where the state of the art sparse coding scheme is alternated with dictionary learning, demonstrates the computational efficiency of the proposed optimization strategy. In addition, the proposed scheme is also seen to be fast and more robust to local minima than the extensions to the greedy K-SVD dictionary learning scheme. More importantly, the ability of the proposed scheme to accommodate Frobenius norm priors is seen to be advantageous in the context of dictionary learning from under sampled data; the number of basis functions that can be reliably learned is limited by the available measurements and signal to noise ratio in this setting. Specifically, this Frobenius norm constraint along with the ℓ_1 sparsity norm results in an implicit model order selection, where the insignificant basis functions are attenuated. We observe that the continuation approach in the majorize-minimize algorithm to be crucial in providing fast convergence. We plan to investigate solving the BCS problem with the augmented Lagrangian approach as proposed in [33], [34] to further improve the algorithm.

The quality of the BCS reconstructions depends on the sparsity regularization parameter λ . In general, in our experiments, the optimal value of λ [based on the metrics in (18) and (19)] did not vary much across datasets acquired with the same protocol (e.g., rest cardiac perfusion MRI, shallow breathing datasets). So, in a practical setting, one could use the same λ tuned for one dataset (based on ground truth data) to recover other datasets from undersampled data that are acquired with the same protocol.

The proposed scheme can be extended in several possible directions. For example, the BCS signal representation can be further constrained by imposing the sparsity of \mathbf{U} in a fixed transform domain (e.g., wavelet, total variation domain) to further reduce the degrees-of-freedom. Since such priors are complementary to the redundancy between the intensity profiles of the voxels exploited by BCS, their use can provide additional gains. This approach is similar in philosophy to [13], where we demonstrated the utility in combining low-rank models with smoothness priors. The adaptation of [35], where the authors used dictionaries with 3-D atoms, may be better than the 1-D dictionaries used in this work. Similarly, the use of motion compensation within the reconstruction scheme as in [36] and [37] can also improve the results. The algorithm was observed to provide good performance with radial sampling trajectories. However, more work is required to evaluate the performance of the algorithm with different sampling trajectories. Since these extensions are beyond the scope of this paper, we plan to investigate these extensions in the future.

V. CONCLUSION

We introduced a novel frame work for blind compressed sensing in the context of dynamic imaging. The model represents the dynamic signal as a sparse linear combination of temporal basis functions from a large dictionary. An efficient majorize-minimize algorithm was used to simultaneously estimate the sparse coefficient matrix and the dictionary. The comparisons of the proposed algorithm with alternate BCS implementations demonstrate the computational efficiency,

insensitivity to initial guesses, and the benefits of combining ℓ_1 sparsity norm with Frobenius norm dictionary constraints. Our phase transition experiments using simulated dynamic MRI data show that the BCS framework significantly outperforms conventional CS methods, and is only marginally worse than the dictionary aware case. This makes the proposed method to be highly useful in dynamic imaging applications where the signal is not sparse in known dictionaries. The validation of the BCS scheme on accelerating free breathing myocardial perfusion MRI show significant improvement over low rank models and compressed sensing schemes. Specifically, the proposed scheme is observed to be robust to spatio-temporal blurring and is efficient in preserving fine structural details.

ACKNOWLEDGMENT

The authors would like to thank the anonymous reviewers for their rigorous and constructive reviews, which considerably improved the quality of the manuscript. The authors acknowledge Dr. E. DiBella from the University of Utah in providing the myocardial perfusion MRI datasets used in this study.

REFERENCES

- [1] Z. Liang, H. Jiang, C. Hess, and P. Lauterbur, "Dynamic imaging by model estimation," *Int. J. Imag. Syst. Technol.*, vol. 8, no. 6, pp. 551–557, 1997.
- [2] Q. Zhao, N. Aggarwal, and Y. Bresler, "Dynamic imaging of time-varying objects," in *Proc. ISMRM*, 2001, p. 1776.
- [3] N. Aggarwal and Y. Bresler, "Patient-adapted reconstruction and acquisition dynamic imaging method (paradigm) for MRI," *Inverse Problems*, vol. 24, no. 4, p. 045015, 2008.
- [4] J. Tsao, P. Boesiger, and K. Pruessmann, "k-t BLAST and k-t sense: Dynamic MRI with high frame rate exploiting spatiotemporal correlations," *Magn. Reson. Med.*, vol. 50, no. 5, pp. 1031–1042, 2003.
- [5] H. Jung, J. Park, J. Yoo, and J. C. Ye, "Radial k-t focuss for high-resolution cardiac cine MRI," *Magn. Reson. Med.*, vol. 63, no. 1, pp. 68–78, Jan. 2010.
- [6] U. Gamper, P. Boesiger, and S. Kozerke, "Compressed sensing in dynamic MRI," *Magn. Reson. Med.*, vol. 59, no. 2, pp. 365–373, 2008.
- [7] M. Lustig, J. Santos, D. Donoho, and J. Pauly, "kt sparse: High frame rate dynamic MRI exploiting spatio-temporal sparsity," in *Proc. 13th Annu. Meet. ISMRM*, Seattle, WA, 2006, p. 2420.
- [8] R. Otazo, D. Kim, L. Axel, and D. Sodickson, "Combination of compressed sensing and parallel imaging for highly accelerated first-pass cardiac perfusion MRI," *Magn. Reson. Med.*, vol. 64, no. 3, pp. 767–776, 2010.
- [9] R. Otazo, D. Kim, L. Axel, and D. Sodickson, "Combination of compressed sensing and parallel imaging with respiratory motion correction for highly-accelerated cardiac perfusion MRI," *J. Cardiovasc. Magn. Reson.*, vol. 13, p. 098, 2011.
- [10] Z. Liang, "Spatiotemporal imaging with partially separable functions," in *Proc. 4th IEEE Int. Symp. Biomed. Imag.: From Nano to Macro*, 2007, pp. 988–991.
- [11] H. Pedersen, S. Kozerke, S. Ringgaard, K. Nehrke, and W. Kim, "k-t PCA: Temporally constrained k-t blast reconstruction using principal component analysis," *Magn. Reson. Med.*, vol. 62, no. 3, pp. 706–716, 2009.
- [12] J. Haldar and Z. Liang, "Spatiotemporal imaging with partially separable functions: A matrix recovery approach," in *IEEE Int. Symp. Biomed. Imag.: From Nano Macro*, 2010, pp. 716–719.
- [13] S. Lingala, Y. Hu, E. DiBella, and M. Jacob, "Accelerated dynamic MRI exploiting sparsity and low-rank structure: k-t SLR," *IEEE Trans. Med. Imag.*, vol. 30, no. 5, pp. 1042–1054, May 2011.
- [14] M. Makowski, C. Jansen, I. Webb, A. Chiribiri, E. Nagel, R. Botnar, S. Kozerke, and S. Plein, "First-pass contrast-enhanced myocardial perfusion MRI in mice on a 3-t clinical MR scanner," *Magn. Reson. Med.*, vol. 64, no. 6, pp. 1592–1598, 2010.
- [15] C. Brinegar, S. Schmitter, N. Mistry, G. Johnson, and Z. Liang, "Improving temporal resolution of pulmonary perfusion imaging in rats using the partially separable functions model," *Magn. Reson. Med.*, vol. 64, no. 4, pp. 1162–1170, 2010.

- [16] B. Zhao, J. Haldar, A. Christodoulou, and Z. Liang, "Image reconstruction from highly undersampled (k, t)-space data with joint partial separability and sparsity constraints," *IEEE Trans. Med. Imag.*, vol. 31, no. 9, pp. 1809–1820, Sep. 2012.
- [17] J. Trzasko, A. Manduca, and E. Borisch, "Local versus global low-rank promotion in dynamic MRI series reconstruction," in *Proc. Int. Symp. Magn. Reson. Med.*, 2011, p. 4371.
- [18] B. Zhao, J. Haldar, C. Brinegar, and Z. Liang, "Low rank matrix recovery for real-time cardiac MRI," in *Biomed. Imag.: From Nano Macro*, 2010, pp. 996–999.
- [19] M. Aharon, M. Elad, and A. Bruckstein, "k-SVD: An algorithm for designing overcomplete dictionaries for sparse representation," *IEEE Trans. Signal Process.*, vol. 54, no. 11, pp. 4311–4322, Nov. 2006.
- [20] S. Ravishanker and Y. Bresler, "MR image reconstruction from highly undersampled k-space data by dictionary learning," *IEEE Trans. Med. Imag.*, vol. 30, no. 5, pp. 1028–1041, May 2011.
- [21] M. Elad and M. Aharon, "Image denoising via sparse and redundant representations over learned dictionaries," *IEEE Trans. Image Process.*, vol. 15, no. 12, pp. 3736–3745, Dec. 2006.
- [22] S. Gleichman and Y. Eldar, "Blind compressed sensing," *IEEE Trans. Inf. Theory*, vol. 57, no. 10, pp. 6958–6975, Oct. 2011.
- [23] M. Lustig, D. Donoho, and J. Pauly, "Sparse MRI: The application of compressed sensing for rapid MR imaging," *Magn. Reson. Med.*, vol. 58, no. 6, pp. 1182–1195, 2007.
- [24] B. Recht, M. Fazel, and P. Parrilo, "Guaranteed minimum-rank solutions of linear matrix equations via nuclear norm minimization," *SIAM Rev.*, vol. 52, no. 3, pp. 471–501, 2010.
- [25] Y. Hu, S. Lingala, and M. Jacob, "A fast majorize-minimize algorithm for the recovery of sparse and low rank matrices," *IEEE Trans. Image Process.*, vol. 21, no. 2, pp. 742–753, Feb. 2012.
- [26] M. Afonso, J. Bioucas-Dias, and M. Figueiredo, "An augmented Lagrangian approach to the constrained optimization formulation of imaging inverse problems," *IEEE Trans. Image Process.*, vol. 20, no. 3, pp. 681–695, Mar. 2011.
- [27] [Online]. Available: http://www.cs.technion.ac.il/~elad/Variables/KSVD_Matlab_ToolBox
- [28] C. Bilen, I. Selesnick, Y. Wang, R. Otazo, D. Kim, L. Axel, and D. Sodickson, "On compressed sensing in parallel MRI of cardiac perfusion using temporal wavelet and TV regularization," in *Proc. 2010 IEEE Int. Conf. Acoust. Speech Signal Process.*, 2010, pp. 630–633.
- [29] P. C. Hansen and D. P. O'Leary, "The use of the l-curve in the regularization of discrete ill-posed problems," *SIAM J. Sci. Comput.*, vol. 14, no. 6, pp. 1487–1503, 1993.
- [30] S. Ramani, T. Blu, and M. Unser, "Monte-Carlo sure: A black-box optimization of regularization parameters for general denoising algorithms," *IEEE Trans. Image Process.*, vol. 17, no. 9, pp. 1540–1554, Sep. 2008.
- [31] S. Ramani, Z. Liu, J. Rosen, J. Nielsen, and J. Fessler, "Magnetic resonance imaging-regularization parameter selection for nonlinear iterative image restoration and MRI reconstruction using GCV and sure-based methods," *IEEE Trans. Image Process.*, vol. 21, no. 8, p. 3659, Aug. 2012.
- [32] S. Lingala and M. Jacob, "A blind compressive sensing frame work for accelerated dynamic MRI," in *Proc. 9th IEEE Int. Symp. Biomed. Imag.*, 2012, pp. 1060–1063.
- [33] S. Ramani and J. Fessler, "Parallel MR image reconstruction using augmented Lagrangian methods," *IEEE Trans. Med. Imag.*, vol. 30, no. 3, pp. 694–706, Mar. 2011.
- [34] S. Lingala, Y. Hu, E. Dibella, and M. Jacob, "Accelerated first pass cardiac perfusion MRI using improved k-t SLR," in *Proc. IEEE Int. Symp. Biomed. Imag.: From Nano to Macro*, 2011, pp. 1280–1283.
- [35] M. Protter and M. Elad, "Image sequence denoising via sparse and redundant representations," *IEEE Trans. Image Process.*, vol. 18, no. 1, pp. 27–35, Jan. 2009.
- [36] S. Lingala, M. Nadar, C. Chefd'hotel, L. Zhang, and M. Jacob, "Unified reconstruction and motion estimation in cardiac perfusion MRI," in *Proc. 2011 IEEE Int. Symp. Biomed. Imag.: From Nano to Macro*, 2011, pp. 65–68.
- [37] H. Jung and J. Ye, "Motion estimated and compensated compressed sensing dynamic magnetic resonance imaging: What we can learn from video compression techniques," *Int. J. Imag. Syst. Technol.*, vol. 20, no. 2, pp. 81–98, 2010.